



# Investigations on physicochemical properties and electrochemical performance of graphite felt and carbon felt for iron-chromium redox flow battery

Huan Zhang<sup>1</sup>  | Na Chen<sup>1</sup> | Chuanyu Sun<sup>2,3</sup>  | Xudong Luo<sup>1</sup>

<sup>1</sup>School of Materials and Metallurgy, University of Science and Technology Liaoning, Anshan, China

<sup>2</sup>School of Materials Science and Engineering, Tianjin University, Tianjin, China

<sup>3</sup>Section of “Chemistry for the Technology” ChemTech, Department of Industrial Engineering, in Department of Chemical Sciences, University of Padova, Padova, Italy

## Correspondence

Huan Zhang, School of Material and Metallurgy, University of Science and Technology Liaoning, Anshan, China.  
Email: zhanghuan@ustl.edu.cn

Chuanyu Sun, School of Materials Science and Engineering, Tianjin University, Tianjin, China. Section of “Chemistry for the Technology” ChemTech, Department of Industrial Engineering, in Department of Chemical Sciences, University of Padova, Padova, Italy.  
Email: chuanyu.sun@aliyun.com

## Funding information

National Natural Science Foundation of China, Grant/Award Number: 51702144; Excellent Talent Training Program of University of Science and Technology Liaoning, Grant/Award Number: 2019RC04; Fundamental Research Funds for the Colleges and Universities in Liaoning Province, Grant/Award Number: 2017LNQN15

## Summary

In this paper, polyacrylonitrile-based graphite felt (GF), carbon felt (CF) and the effect of thermal activation on them with or without the catalyst ( $\text{BiCl}_3$ ) are comprehensively investigated for iron-chromium redox flow battery (ICRFB) application. The physical-chemical parameters of GF and CF after the thermal activation is affected significantly by their graphitization degree, oxygen functional groups, and surface area. Cyclic voltammetry (CV) and electrochemical impedance spectroscopy (EIS) results manifest that GF and CF before and after the thermal activation have different electrocatalytic activities owing to oxygen functional groups number increase and the graphitization degree decrease. In terms of the capacity decay rate, as oxygen functional groups provide shorter electrocatalytic pathways than bismuth ions, the performance of GF and CF after the thermal activation is more ideal. As a result, GF before and after the thermal activation exhibits higher efficiency (EE: 86%) and better stability at a charge-discharge current density of  $60 \text{ mA}\cdot\text{cm}^{-2}$  than those of CF during charge-discharge cycling, as the dominant limitation in an ICRFB is ohmic and activation polarization. Therefore, GF after thermal activation together with the addition of  $\text{BiCl}_3$  in the electrolyte is a more promising electrode material for ICRFBs application than CF.

## KEYWORDS

carbon felt, graphite felt, graphitization degree, iron-chromium redox flow battery (ICRFB), thermal activation

## 1 | INTRODUCTION

Nowadays, with the intensification of the fossil fuel crisis, renewable energy has become the core issue of the times. However, the renewable energy resources, for instance,

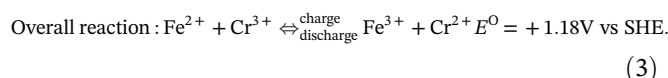
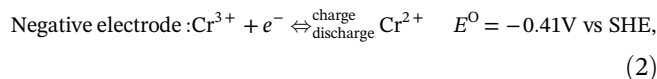
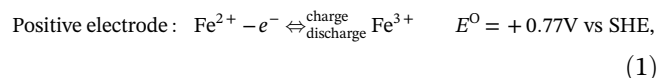
solar and wind, have the unstable and low-quality output of electricity based on its random and intermittent nature, which further affects the grid stability. The energy storage system (ESS), which serves as a temporary intermediary to accumulate and release energy as

required, consequently, proves to be a feasible solution to tackle these issues. According to the cost and performance requirement, electrochemical ESS or secondary batteries are turning into a desired choice for ESS as a result of their superiorities, such as low environmental footprint, quite large power rate and control window for capacity, the ability to be installed anywhere, not being limited by geographical requirement, and fast response time.<sup>1</sup>

For the large-scale ESS, redox flow battery (RFB) with the superiorities of high safety, long cycle life, flexible design, and low cost of maintenance makes it an emerging high-efficiency technology.<sup>2</sup> It takes advantage of the soluble active substances in the form of various oxidation states to accumulate and release chemical potential energy by reversible redox reactions. One of the most important characteristics of RFB is the feasibility of an independent scaling-up of the power portion (electrochemical cell) and electric energy storage portion (external tanks). The energy storage capacity of an RFB can be enhanced by simply increasing the volume of the electrolytes and/or the concentration of the electroactive species, which is a strong point over other ESS techniques.<sup>3,4</sup>

The iron-chromium redox flow battery (ICRFB) was widely studied by NASA in the 1970s, and it was the first true RFB in the world.<sup>5</sup> An emblematical RFB system is made up of a flow circulation system, a membrane separator, two electrodes, and two exterior tanks that lay up dissolved electroactive electrolytes. The oxidation of  $\text{Fe}^{2+}$  species to  $\text{Fe}^{3+}$  species takes place in the positive half-cell during the charging process, and the reduction of  $\text{Cr}^{3+}$  species to  $\text{Cr}^{2+}$  occurs in the negative half-cell, while during the discharge operation of the battery, reversed

processes of the reactions described above arise. The detailed electrochemical redox reactions during charge-discharge cycling were shown as follows<sup>6</sup>:



Generally, carbon materials are considered as desirable electrode materials for the application of ICRFB owing to their reasonable cost, high chemical stability, long cycle life, and wide operational potential range in highly oxidizing media. A variety of carbon materials, for instance, graphite felt (GF), carbon paper (CP), and carbon felt (CF), have been studied as the electrodes for ICRFBs.<sup>7-11</sup> While because of the larger specific surface area and better three-dimensional network structures, as well as high chemical stability and electrical conductivity, polyacrylonitrile (PAN)-based GF and CF are preferable electrode materials.<sup>12-14</sup>

The production of PAN-based GF and CF includes three main steps: stabilization, carbonization, and graphitization.<sup>15,16</sup> The specific production process steps and the evolution of the GF and CF structure during the preparation process are shown in Figure 1. The most significant structural transformations occur during the

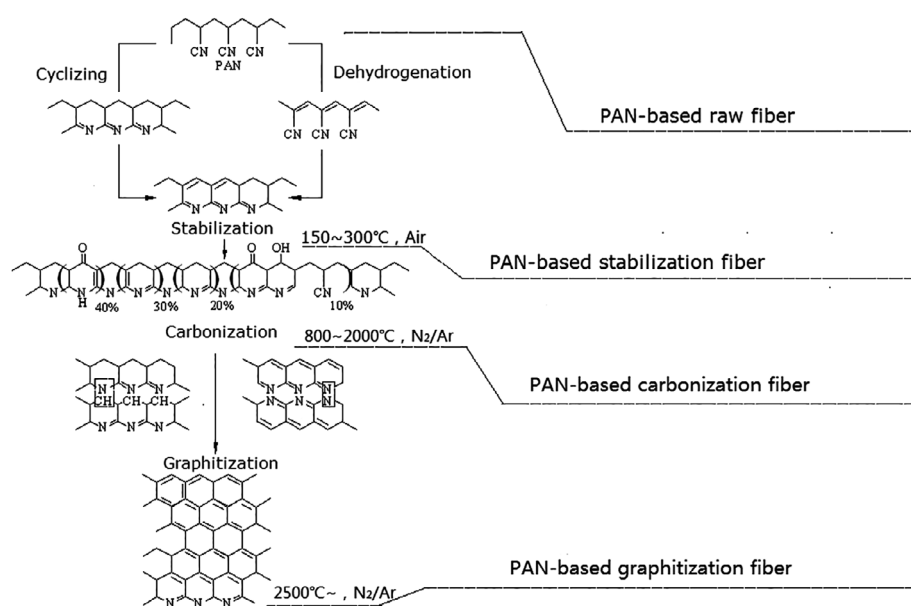


**FIGURE 1** Production processes and structural evolution of PAN-based fiber (reproduced from Fizer and Heine<sup>15</sup>). PAN, polyacrylonitrile

carbonization step. All of these manufacturing steps could theoretically result in delicate distinctions in the end products, especially considering that PAN-based GF or CF producers only specify a range of their products' bulk physical properties (eg, thickness, porosity, bulk density, and thermal conductivity).<sup>17</sup> However, researchers have made efforts to enhance PAN-based GF or CF during the modification process. It is reported that more than 100 articles had been published, which is bound up with the surface treatments of GF and CF electrodes up until 2018, such as thermal activation, acid treatment, and metal doping.<sup>13</sup> More and more researchers are attempting various means for enhancing the electrochemical activity of GF or CF electrode.<sup>18-23</sup>

The influence of GF and CF on the performance of vanadium redox flow battery (VRFB) has been widely reported,<sup>24-27</sup> while there is less literature on this issue for the application of ICRFBs, as shown in Table S1. Liu et al reported that in comparison with GF, the VRFB adopted with CF exhibits much higher electrochemical activity.<sup>14</sup> As the electrode reactions of ICRFB are significantly different from VRFB, it may be essential to investigate the difference of physicochemical properties between GF and CF on the ICRFB performance, which may further give the reader a guideline for the selection of optimal electrode material. In this paper, commercial PAN-based GF and CF are compared with the electrochemical performance in ICRFBs. As we have seen, to date, there is no report in the literature intuitively contrasting the application behavior of PAN-based GF and CF electrodes in ICRFBs. Thermal activation and the catalyst ( $\text{BiCl}_3$ ), which are selected most in ICRFBs reportedly,<sup>6,28-31</sup> are employed to evaluate their effects on the electrochemical activities of GF and CF.

## 2 | EXPERIMENTAL

### 2.1 | Materials

The PAN-based GFs and CFs were procured from Gansu Haoshi Carbon Fiber Co., Ltd., China. The graphitization temperature of GF was 2500°C, and the carbonation temperature of CF was 1800°C. The thickness of pristine felts was 5 mm, and the felts were denoted as GF and CF, respectively. Then, GF and CF were further activated by thermal treatment at 500°C in the air for 5 hours, which were denoted as T-GF and T-CF, respectively.

### 2.2 | Physical measurements

The morphology of the samples was characterized by employing a Zeiss-Sigma-HD scanning electron

microscopy (SEM). The fiber diameter was measured by SEM images, and about 20 monofilaments were randomly selected from each sample. The fiber diameter size was obtained from the SEM image, and the average value was taken. The crystal structure of each electrode was examined by X-ray diffraction (X'pert Powder) with a  $\text{CuK}_\alpha$  source ( $\lambda = 0.15406 \text{ nm}$ ). A DXR Raman microscope spectrometer was applied for the measurement of Raman spectroscopy. The shift range of Raman was set between 50 and 3500  $\text{cm}^{-1}$ ; the selected laser wavelength by using argon ion was 514.5 nm; the spot diameter, spectral resolution, and objective lens were 5 mm, 1  $\text{cm}^{-1}$ , and 20 times, respectively. To investigate the surface composition of each felt, ESCALAB 250xi X-ray photoelectron spectroscopy (XPS) was adopted for the characterization. An Al Ka X-ray source of microfocus monochromatic with the spot diameter of 500  $\mu\text{m}$  and energy of 1486.6 eV was applied for the measurement of all the samples. For the broad-spectrum mode, the scanning power was set as 100 eV, while for the narrow spectrum, the power was set as 20 eV. The C 1s peak of hydrocarbons with a binding energy of 285.0 eV was selected for the calibration of all the spectra. The Brunauer-Emmett-Teller (BET) surface area was ascertained via the  $\text{N}_2$  adsorption-desorption approach at  $-196.15^\circ\text{C}$  after the degassing process at  $150^\circ\text{C}$  for 3 hours (Quantachrom Autosorb-iQ2 system). The thermogravimetric analysis (TGA)/differential scanning calorimetry (DSC) curves of samples were carried out by using a thermogravimetric analyzer (Netzsch STA449 F3). The obtained electrodes were situated in a ceramic supporter, heated from an initial temperature of  $45^\circ\text{C}$  up to  $1000^\circ\text{C}$  at a constant rate of  $5^\circ\text{C}\cdot\text{min}^{-1}$  in an air atmosphere with a constant flow rate of  $200 \text{ mL}\cdot\text{min}^{-1}$ .

### 2.3 | Electrochemical measurements

The electrochemical results were obtained by employing the Corrtest-CS310H (Wuhan Corrtest) workstation in  $1.0 \text{ mol}\cdot\text{L}^{-1}\text{CrCl}_3 + 1.0 \text{ mol}\cdot\text{L}^{-1}\text{FeCl}_2 + 3.0 \text{ mol}\cdot\text{L}^{-1}\text{HCl}$  solution or  $1.0 \text{ mol}\cdot\text{L}^{-1}\text{CrCl}_3 + 1.0 \text{ mol}\cdot\text{L}^{-1}\text{FeCl}_2 + 3.0 \text{ mol}\cdot\text{L}^{-1}\text{HCl} + 8 \text{ mmol}\cdot\text{L}^{-1}\text{BiCl}_3$  solution at room temperature. All the electrochemical analyses were conducted in an electrolytic cell with a three-electrode system, which was utilized with the prepared electrode materials ( $0.4 \text{ cm}^2$ ) as the working electrode, a saturated calomel electrode (SCE) as the reference electrode and the Pt plate ( $1.0 \text{ cm}^2$ ) as the counter electrode. Cyclic voltammetry (CV) curves were obtained over the voltage range from  $-1.0$  to  $0.8 \text{ V}$  with a scan rate of  $3 \text{ mV/s}$ . Electrochemical impedance spectroscopy (EIS) was measured in the amplitude of the alternating

voltage of 5 mV over the frequency ranging from  $10^{-2}$  to  $10^5$  Hz.

The performances of single cells were tested in dynamic ICRFBs. A perfluorinated ion-exchange membrane Nafion 115 was employed as the separator, which has been pretreated as reported in the literature.<sup>32,33</sup> Two pieces of felts were the electrodes (active area of  $9\text{ cm}^2$ ), and graphite plates were current collectors. The cell was assembled by sealing the three components (membrane, electrode, and plate) with silicone rubber as gaskets. The catholyte was composed of 50-mL solution containing  $1.0\text{ mol} \cdot \text{L}^{-1}\text{CrCl}_3 + 1.0\text{ mol} \cdot \text{L}^{-1}\text{FeCl}_2 + 3.0\text{ mol} \cdot \text{L}^{-1}\text{HCl}$ , and the anolyte was composed of 50-mL solution containing  $1.0\text{ mol} \cdot \text{L}^{-1}\text{CrCl}_3 + 1.0\text{ mol} \cdot \text{L}^{-1}\text{FeCl}_2 + 3.0\text{ mol} \cdot \text{L}^{-1}\text{HCl} + 8.0\text{ mmol} \cdot \text{L}^{-1}\text{BiCl}_3$ . The catholyte and anolyte were stored in tanks outside the cells and cyclically pumped into the relevant component portion during the operation. The active solution flows through a magnetic circulating pump with a flow rate of  $100\text{ mL} \cdot \text{min}^{-1}$  (MP-10R, Shanghai Zhiwo pump valve Co. LTD, China). The mean linear electrolyte flow velocity past the surface of the electrode is calculated based on literature,<sup>34</sup> which is equal to  $1.74\text{ cm} \cdot \text{s}^{-1}$ . The entire single cell was situated

in a temperature control oven, which may further assure the practical temperature during the single-cell operation was kept at  $65^\circ\text{C}$ . The cells were monitored by a CT2001C-5V/2A (Wuhan Land Co., China) charge-discharge tester at the current density of  $60\text{ mA} \cdot \text{cm}^{-2}$  and voltage window between 0.8 and 1.2 V.

### 3 | RESULT AND DISCUSSION

#### 3.1 | Characterization

The morphology of the samples is reported in Figure 2. The surface of GF (Figure 2A) is cleaner than CF (Figure 2B), where a large number of coarse ravines can be observed on both of them. Meanwhile, there is no significant difference in the diameters of the two fibers because of the different carbonization or graphitization temperature; that is, both the diameters of the two fibers are between 9 and  $10\text{ }\mu\text{m}$ . Besides, BET surface areas of GF and CF are very low ( $<2\text{ m}^2 \cdot \text{g}^{-1}$ ), as shown in Table 1. However, thermal treatment makes a big difference in the morphology of T-GF (Figure 2C) and T-CF (Figure 2D). In Figure 2A,C, compared with GF, the

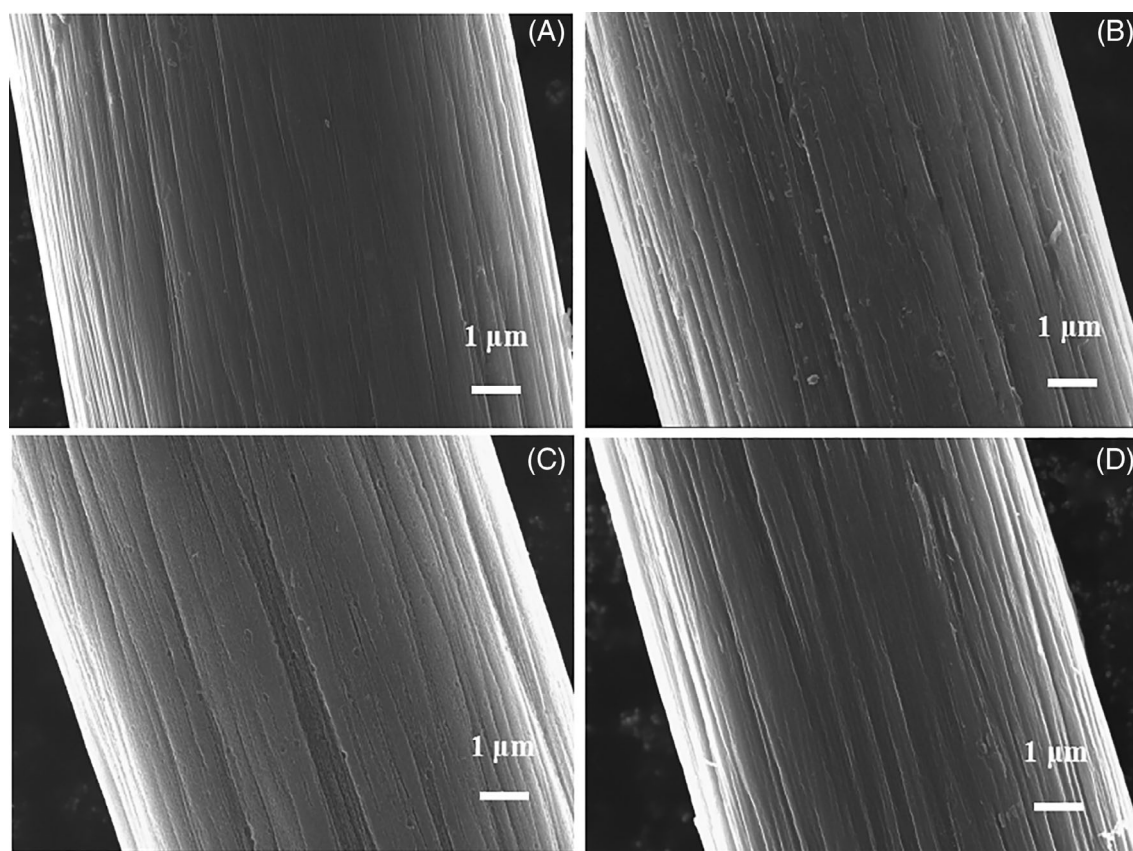


**FIGURE 2** SEM images of (A) GF, (B) CF, (C) T-GF, and (D) T-CF. CF, carbon felt; GF, graphite felt; SEM, scanning electron microscopy

**TABLE 1** Physical-chemical parameters of samples

Sample	BET, $\text{m}^2\cdot\text{g}^{-1}$	$I_D/I_G$	C at %	O at %	N at %
GF	<2	0.77	95.33	4.11	0.55
CF	<2	1.44	94.19	5.34	0.39
T-GF	8.66	1.47	91.87	7.56	0.58
T-CF	13.67	1.81	91.63	7.53	0.84

Abbreviations: CF, carbon felt; GF, graphite felt.

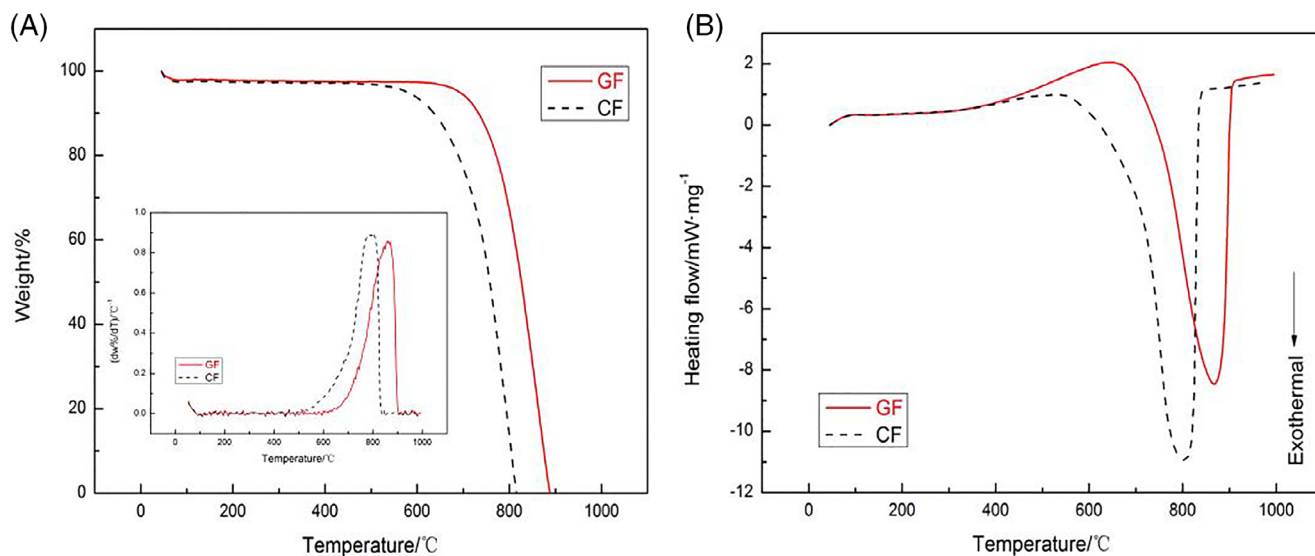


**FIGURE 3** TGA and DTA (A) and DSC (B) curves of GF and CF. CF, carbon felt; DSC, differential scanning calorimetry; DTA, differential thermal analysis; GF, graphite felt; TGA, thermogravimetric analysis [Colour figure can be viewed at [wileyonlinelibrary.com](http://wileyonlinelibrary.com)]

diameter of T-GF does not decrease significantly, and only nano-sized micropores appear on the surface of the fibers. In contrast, in Figure 2B,D, the surface of the T-CF fibers is slightly changed, but the fiber diameter of T-CF reduces by approximately 7.5%. The BET surface area of GF increases by about 4 times ( $8.63 \text{ m}^2\cdot\text{g}^{-1}$ ) after 5-hour treatment of hot air at  $500^\circ\text{C}$ . However, under the same thermal activation conditions, the surface area of CF increases by about 6 times ( $13.67 \text{ m}^2\cdot\text{g}^{-1}$ ).

The thermal analysis results of GF and CF are shown in Figure 3. It can be seen from Figure 3A that the initial temperature of weight loss in CF is lower than GF. The GF remains thermally stable up to approximately  $650^\circ\text{C}$ , and the total weight loss is only 3.4% by mass. The differential thermal analysis (DTA) curves in the inset of Figure 3A further reflect that the thermal treatment exerts more influence on the thermal stability of CF than GF. The DSC curves of GF and CF are displayed in Figure 3B. The heat profile of CF reveals a single well-defined transition temperature at  $802.6^\circ\text{C}$ , while  $866.6^\circ\text{C}$  for GF. Meanwhile, the maximum heat release of CF is larger than that of GF (CF is  $-6669 \text{ J}\cdot\text{g}^{-1}$ ; GF is  $-7844 \text{ J}\cdot\text{g}^{-1}$ ). The above results indicate that CF is more

susceptible to the oxidation of hot air than GF. The tendency is consistent with the result of morphology on the surface of the samples after thermal treatment.

The XRD results of each sample are shown in Figure 4, wherein the peak at  $2\theta \approx 25^\circ$  corresponds to the crystal plane of (0 0 2). The characteristic peak at  $2\theta \approx 44^\circ$  is a small peak, which is analogous to the overlaying of the corresponding characteristic reflections of (1 0 0) crystal plane of the low-ordered carbon in GF and CF.<sup>35</sup> In addition, the weak peaks at  $2\theta \approx 53^\circ$  correspond to the (0 0 4) crystal plane, and the characteristic peaks at  $2\theta \approx 78^\circ$  are the diffraction peaks of the (1 1 0) crystal plane.<sup>36</sup> Both GF and T-GF demonstrate sharper characteristic peaks and the displacement of (0 0 2) toward the higher angles, which indicates that CF and T-CF have more structural defects, including defective carbon or edge carbon, as shown in Scheme 1.

The graphitization degree of the electrodes may be preferably ascertained by Raman spectroscopy, as revealed by Figure 5. In Figure 5, two characteristic peaks in the Raman spectra of samples are presented: (a) the D peak at approximately  $1350 \text{ cm}^{-1}$  is derived from the vibration of the  $\text{sp}^3$  hybrid bond at the disordered grain boundary or other

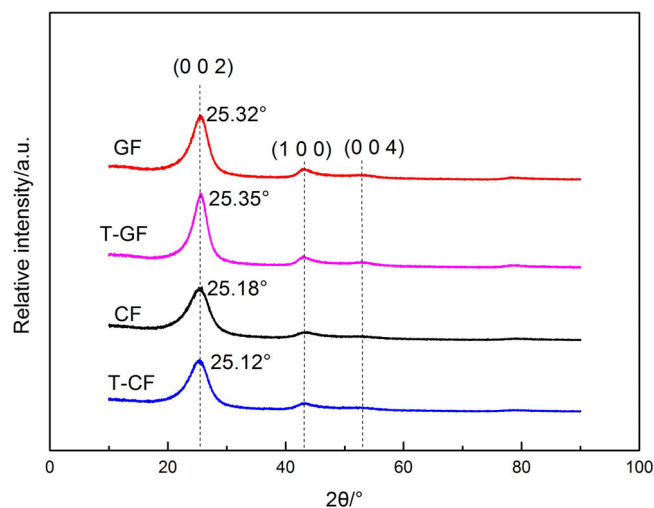
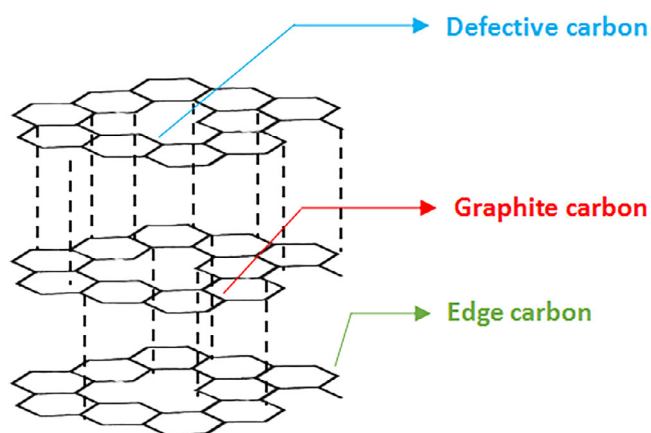


**FIGURE 4** XRD patterns of samples. XRD, X-ray diffraction



**SCHEME 1** Crystal unit of GF/T-GF or CF/T-CF. CF, carbon felt; GF, graphite felt [Colour figure can be viewed at [wileyonlinelibrary.com](http://wileyonlinelibrary.com)]

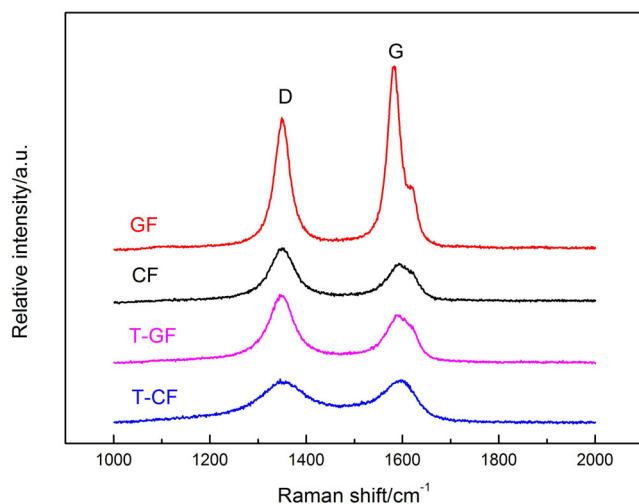


**FIGURE 5** Raman spectra of samples. CF, carbon felt; GF, graphite felt

structural defects in the felt; (b) the G peak at approximately  $1580\text{ cm}^{-1}$  is caused by the stretching vibration of the  $\text{sp}^2$  hybrid bond of the adjacent carbon atoms in the plane of the carbon network in the felt.<sup>37,38</sup> Therefore, the relative intensity ratio of the D and G peaks ( $I_D/I_G$ ) is often used to determine the graphitization degree of the felt electrode and the integrity of the crystal structure (see Scheme 1). The smaller the  $I_D/I_G$  value, the higher the graphitization degree of the felt electrode. That means, the larger the  $I_D/I_G$  value, the smaller the proportion of the regular structure in the felt electrode. The  $I_D/I_G$  results of each sample are described in Table 1. From Table 1, it can be concluded that the degree of graphitization in the structure of GF is found greater than CF, which is identical to the results of XRD. However, after the activation by hot air, compared with GF and CF, the  $I_D/I_G$  values of T-GF and T-CF increased. Simultaneously, the  $I_D/I_G$  ratio of T-CF is larger than that of T-GF. Raman on carbon materials has only an information depth of about 50 nm, whereas XRD probes the whole fiber volume. Therefore, the above results reveal that hot air makes the surface of the fibers an increase in the amount of defective carbon or edge carbon. This phenomenon may further illustrate that the hot air is more oxidative to the surface of CF with more defective carbon structure and the oxidation reaction is easier for that of CF.

The number of C, O, and N atoms in each sample which is obtained by XPS results is reported in Table 1. The atomic content of each element listed in Table 1 is derived directly from the percentage of the integrated area of each fine spectrum in the XPS test. The integral areas of the characteristic peaks for the samples were obtained by Gaussian or Lorentz fitting to the fine spectrum of C, N, and O elements, and the atomic-specific content of the three elements was calculated. Because of the difference in the graphitization degree on the surface of fibers, the amount of C atoms in GF is larger than CF, while the amount of O atoms is smaller. Concurrently, the thermal treatment brings about a decrease in the number of C atoms in T-CF and T-GF by varying degrees, while the number of O atoms increases. Further peak fitting of the C 1s and O 1s peaks for each sample is shown in Figure 6, and the fitting results are shown in Table 2. Among them, the C 1s spectra is fitted at five peaks of 284.1, 285, 285.96, 288.2, 290.4, and 291.61 eV, corresponding to C=C bond (graphite carbon), C—C bond (defective carbon), C—O—H bond, C=O bond, O=C—OH bond, and  $\pi$ - $\pi^*$ , respectively.<sup>39</sup> The O 1s spectra have been split into three peaks at 531.8, 533, and 535 eV, respectively, which is analogous to the binding energies of C=O groups, C—OH/C—O—C groups, and ether-like species.<sup>40</sup> From the quantitative results of XPS, it can be seen that the thermal treatment reduces the number of graphite carbon (C=C) of T-GF and T-CF.

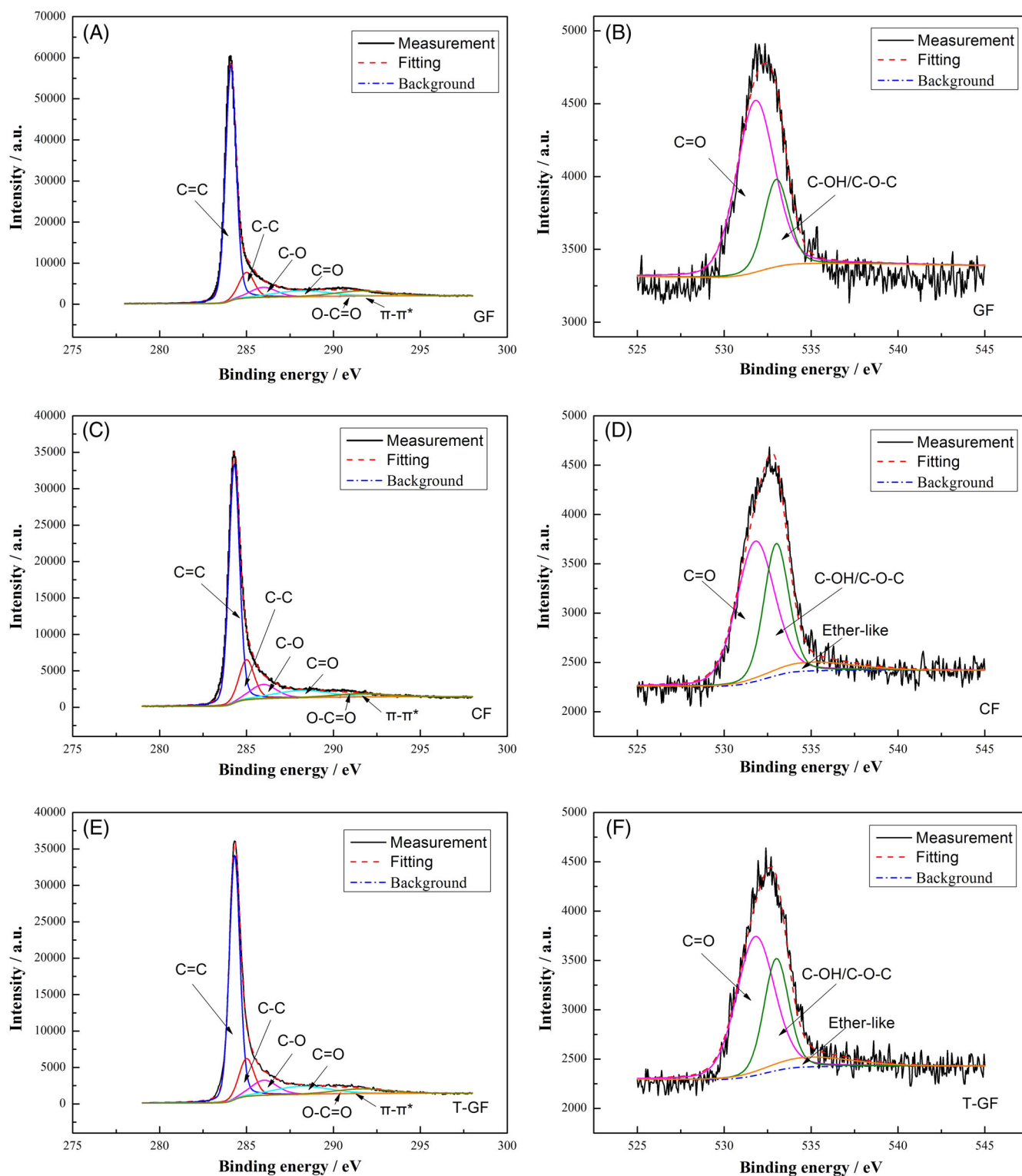


**FIGURE 6** C 1s and O 1s XPS fitting of (a, b) GF, (c, d) CF, (e, f) T-GF, and (g, h) T-CF. CF, carbon felt; GF, graphite felt; XPS, X-ray photoelectron spectroscopy [Colour figure can be viewed at [wileyonlinelibrary.com](http://wileyonlinelibrary.com)]

Compared with GF and CF, the decreases in the number of C=C of T-GF and T-CF are approximately 12% and 18%, respectively. This result further confirms that the reason for the decrease in the ordering degree on the

surface of the T-CF is attributed to carbon net destroyed. However, the increases in the number of defective carbon (C—C) and unsaturated carbon (C—O—H and C=O) in T-CF (approximately 20% and 17%) are less compared with

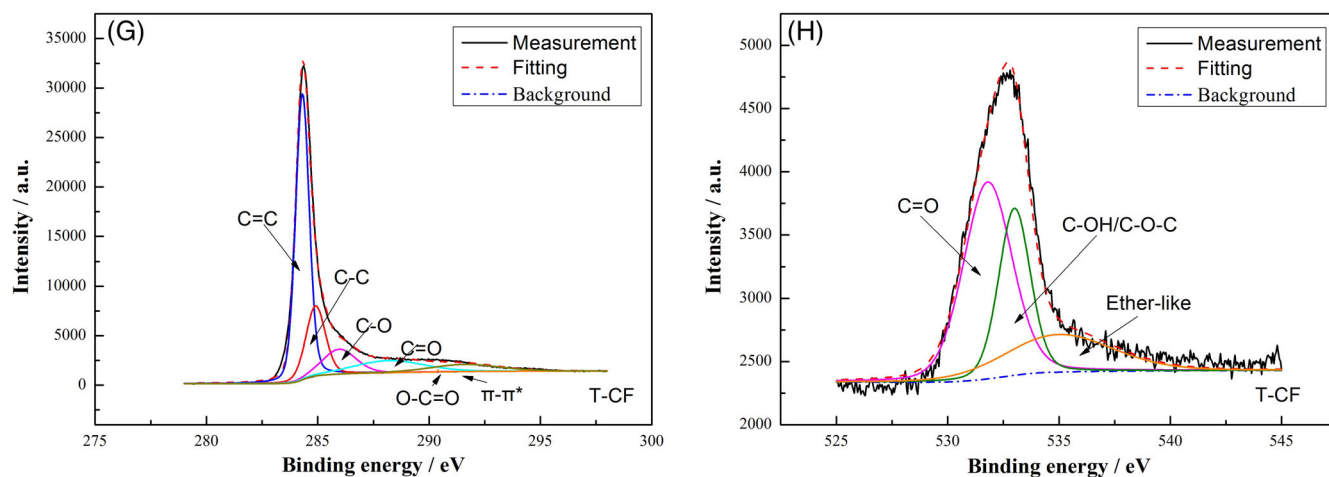


FIGURE 6 (Continued)

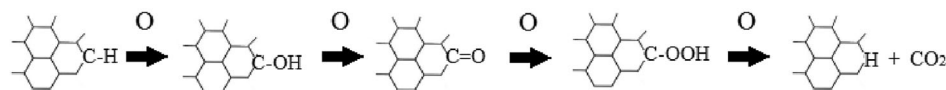
TABLE 2 Functional groups obtained from C 1s and O 1s spectra peak fitting of samples

Samples	C 1s (%)					
	C=C (284.1 eV)	C-C (285 eV)	C-O (285.96 eV)	C=O (288.2 eV)	O-C=O (290.4 eV)	$\pi$ - $\pi^*$ (291.61 eV)
GF	63.21	9.86	6.69	8.46	0.003	7.10
CF	58.30	14.00	8.54	9.25	0.003	4.08
T-GF	55.94	12.41	8.49	9.58	0.003	5.44
T-CF	47.84	16.84	10.27	10.55	0.002	6.13

Samples	O 1s (%)		
	C=O (531.8 eV)	C-OH/C-O-C (533 eV)	Ether-like (535 eV)
GF	3.08	1.03	-
CF	3.05	1.87	0.42
T-GF	4.49	2.37	0.70
T-CF	3.80	2.14	1.62

Abbreviations: CF, carbon felt; GF, graphite felt.



**SCHEME 2** Oxidation process of unsaturated carbon (reproduced from Yue et al<sup>41</sup>)

that of T-GF (approximately 26% and 19%). The more complete structure of GFs carbon net structure makes it easier for hot air to attack the edge carbon. The process of oxidation of GF in hot air until weight loss takes place is closer to Scheme 2. Whereafter, XPS results illustrate that the existing form of the oxygen functional groups in GF and CF is similar; that is, the C=O group is the most, followed C-OH/C-O-C group. Although the number of C=O and C-OH/C-O-C groups in both T-GF and T-CF increased, there were more C-OH/C-O-C group in

T-GF and some oxygen to be converted to ether-like species in T-CF.

### 3.2 | CV and EIS analysis

The CV curve of each sample is reported in Figure 7, and the scanning rate is set as  $3 \text{ mV}\cdot\text{s}^{-1}$ . The electrolyte is  $1.0 \text{ mol}\cdot\text{L}^{-1} \text{FeCl}_2 + 1.0 \text{ mol}\cdot\text{L}^{-1} \text{CrCl}_3 + 3.0 \text{ mol}\cdot\text{L}^{-1} \text{HCl}$  solution in Figure 7A. The redox peaks appearing in



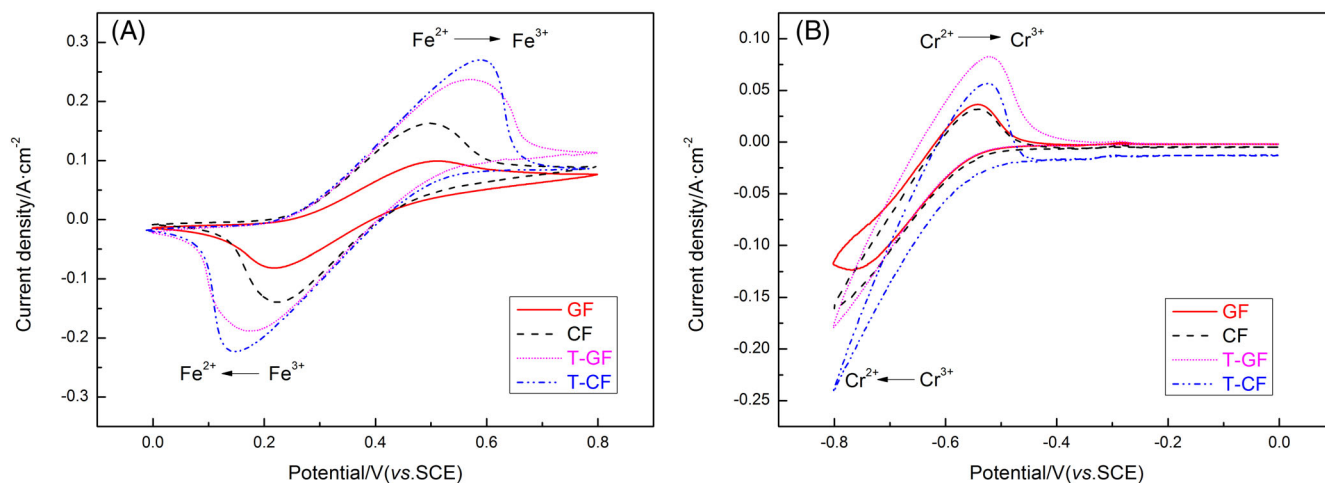


**FIGURE 7** Cyclic voltammetry at a scan rate of  $3 \text{ mV} \cdot \text{s}^{-1}$  in (A)  $1.0 \text{ mol} \cdot \text{L}^{-1} \text{CrCl}_3 + 1.0 \text{ mol} \cdot \text{L}^{-1} \text{FeCl}_2 + 3.0 \text{ mol} \cdot \text{L}^{-1} \text{HCl}$  and (B)  $1.0 \text{ mol} \cdot \text{L}^{-1} \text{CrCl}_3 + 1.0 \text{ mol} \cdot \text{L}^{-1} \text{FeCl}_2 + 3.0 \text{ mol} \cdot \text{L}^{-1} \text{HCl} + 8.0 \text{ mmol} \cdot \text{L}^{-1} \text{BiCl}_3$ . CF, carbon felt; GF, graphite felt [Colour figure can be viewed at [wileyonlinelibrary.com](http://wileyonlinelibrary.com)]

**TABLE 3** Parameters obtained from Figure 7A for the positive redox couple

Sample	$E_{\text{pa}}$ , mV	$E_{\text{pc}}$ , mV	$I_{\text{pa}}$ , $\text{A} \cdot \text{cm}^{-2}$	$I_{\text{pc}}$ , $\text{A} \cdot \text{cm}^{-2}$	$\Delta E$ , mV	$I_{\text{pa}}/I_{\text{pc}}$
GF	511	218	0.10	0.09	293	1.11
CF	496	225	0.16	0.17	271	0.94
T-GF	570	175	0.22	0.30	395	0.73
T-CF	590	148	0.27	0.31	442	0.87

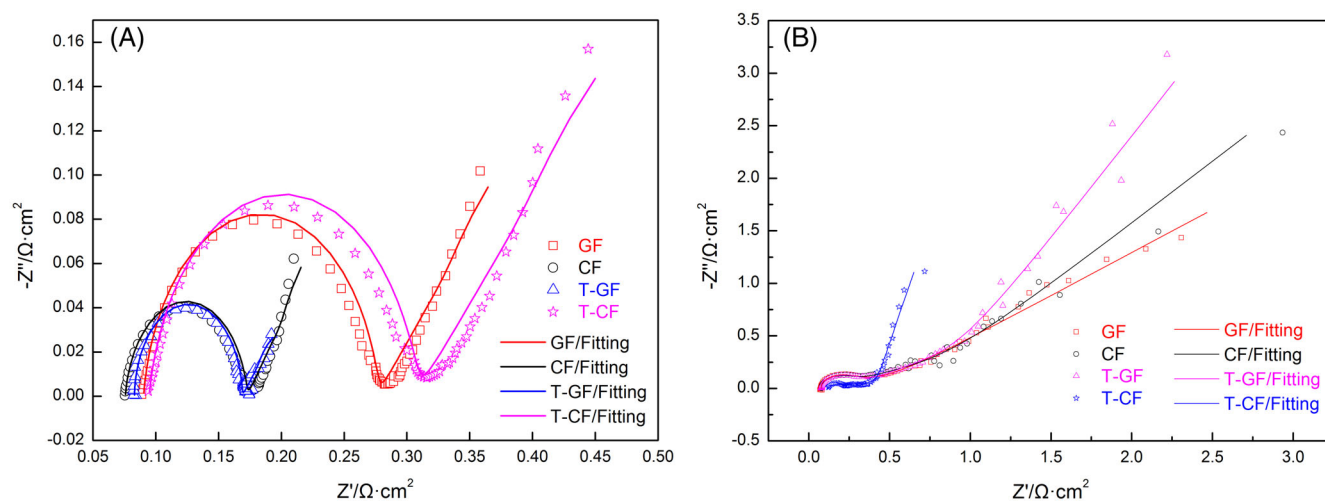
Abbreviations: CF, carbon felt; GF, graphite felt.

Figure 7A correspond to the redox reaction of the  $\text{Fe}^{2+}/\text{Fe}^{3+}$  couple in the positive reaction, and the obtained reaction kinetic parameters are listed in Table 3. CF exhibits higher electrocatalytic activity than GF for the positive reaction. After thermal treatment of GF and CF, the reduction peak current ( $I_{\text{pc}}$ ) and the oxidation peak current ( $I_{\text{pa}}$ ) of T-GF and T-CF are significantly improved. The relationship between the peak current ( $I_{\text{p}}$ ) and each parameter is as shown in Equation (4)<sup>42</sup>:

$$I_{\text{p}} = 2.99 \times 10^5 A n^3 C_0 (\alpha D_0 v)^{\frac{1}{2}}, \quad (4)$$

where  $C_0$  (the unit:  $\text{mol} \cdot \text{L}^{-1}$ ) stands for the concentration of the solution;  $D_0$  (the unit:  $\text{cm}^2 \cdot \text{s}^{-1}$ ) is the diffusion coefficient;  $v$  (the unit:  $\text{mV} \cdot \text{s}^{-1}$ ) represents the scanning rate;  $A$  (the unit:  $\text{cm}^2$ ) stands for the area of the electrode;  $n$  represents the number of transferred electrons during the redox reaction, which is taken as 1 in our case;  $\alpha$  represents the transfer coefficient. Therefore, the peak current is related to the area of the electrode. Previous BET results confirm that thermal activation method enlarges the surface area of T-GF and T-CF; thus, a large peak current is generated on the

surfaces of T-GF and T-CF. From the change of the peak current ratio ( $I_{\text{pa}}/I_{\text{pc}}$ ), the symmetry of the CV curve of each sample is not ideal.<sup>43</sup> Moreover, the peak position and also the difference of peak positions in CV measurements are controlled by electrode and diffusion kinetics. As showed in Figure 7A, T-GF and T-CF have a relatively lower onset potential for the electrochemical reactions despite their significant difference of peak potential ( $\Delta E$ ). Therefore, the increase in peak difference of T-GF and T-CF is rather caused by diffusion limitations.<sup>44</sup> In order to further catalyze the negative reaction, the electrolyte environment of Figure 7B is  $1.0 \text{ mol} \cdot \text{L}^{-1} \text{CrCl}_3 + 1.0 \text{ mol} \cdot \text{L}^{-1} \text{FeCl}_2 + 3.0 \text{ mol} \cdot \text{L}^{-1} \text{HCl} + 8.0 \text{ mmol} \cdot \text{L}^{-1} \text{BiCl}_3$ , and the only oxidation peak appearing obviously in the figure corresponds to the oxidation reaction of the negative  $\text{Cr}^{3+}/\text{Cr}^{2+}$  couple.<sup>6</sup> There is little difference in the peak current between CF and GF. Similar to the result of the positive reaction, the increase of the surface area of T-CF and T-GF further enlarges the peak current density of the negative reaction. Meanwhile, the reduction peak currents of the samples in  $-0.8 \text{ V}$  (vs SCE) position display that  $I_{\text{pc}}(\text{T-CF}) > I_{\text{pc}}(\text{T-GF}) > I_{\text{pc}}(\text{CF}) > I_{\text{pc}}(\text{GF})$ . Therefore, the increase in the number of oxygen functional groups of



**FIGURE 8** EIS spectroscopy and fitting curves at 0.4 V (vs SCE) in (A)  $1.0 \text{ mol} \cdot \text{L}^{-1} \text{FeCl}_2 + 1.0 \text{ mol} \cdot \text{L}^{-1} \text{CrCl}_3 + 3.0 \text{ mol} \cdot \text{L}^{-1} \text{HCl}$  solution and  $-0.5 \text{ V}$  (vs SCE) in (B)  $1.0 \text{ mol} \cdot \text{L}^{-1} \text{FeCl}_2 + 1.0 \text{ mol} \cdot \text{L}^{-1} \text{CrCl}_3 + 3.0 \text{ mol} \cdot \text{L}^{-1} \text{HCl} + 8.0 \text{ mmol} \cdot \text{L}^{-1} \text{BiCl}_3$  solution. EIS, electrochemical impedance spectroscopy; SCE, saturated calomel electrode [Colour figure can be viewed at [wileyonlinelibrary.com](http://wileyonlinelibrary.com)]

**TABLE 4** The parameters obtained from fitting the EIS plots with the equivalent circuit

Sample	$\eta(\text{V})$	$R_s, \Omega \cdot \text{cm}^2$	CPE-T	CPE-P	$R_{ct}, \Omega \cdot \text{cm}^2$	W-R	W-T	W-P
GF	0.4	0.090	0.003	0.921	0.186	0.305	96.530	0.506
CF	0.4	0.076	0.006	0.921	0.097	0.164	77.850	0.561
T-GF	0.4	0.083	0.004	0.980	0.086	0.068	65.940	0.528
T-CF	0.4	0.095	0.003	0.901	0.213	0.463	96.290	0.493
Samples	$\eta(\text{V})$	$R_s, \Omega \cdot \text{cm}^2$	CPE-T	CPE-P	$R_{ct}, \Omega \cdot \text{cm}^2$	W-R	W-T	W-P
GF	$-0.5$	0.077	6.629E-4	1.090	0.078	0.879	1.319	0.220
CF	$-0.5$	0.080	6.941E-4	1.090	0.091	1.642	5.005	0.278
T-GF	$-0.5$	0.079	1.987E-3	0.999	0.193	1.609	5.832	0.351
T-CF	$-0.5$	0.077	6.790E-2	0.399	0.236	0.323	3.674	0.436

Abbreviations: CF, carbon felt; GF, graphite felt; EIS, electrochemical impedance spectroscopy.

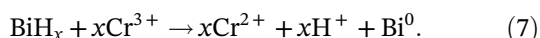
T-GF and T-CF caused by hot air can be recognized as an effective mean to improve electrode activity in ICRFBs.<sup>45-47</sup>

Figure 8 compares EIS spectra of each sample at polarization overpotential ( $\eta$ ) of 0.4 V (vs SCE) (Figure 8A) and  $-0.5 \text{ V}$  (vs SCE) (Figure 8B). In Figure 8, all EIS spectra are composed of a semicircle and linear parts. It is proved that under the corresponding polarization overpotential, the redox reactions of  $\text{Fe}^{2+}/\text{Fe}^{3+}$  and  $\text{Cr}^{3+}/\text{Cr}^{2+}$  couples that take place on the surface of each sample are mainly due to the effect of charge transfer (semicircle part) and diffusion (linear part).<sup>43</sup> All the EIS spectra are fitted according to the equivalent circuit in Figure 8, where  $R_s$  represents ohmic resistance, ie, the sum of the electrode resistance and solution resistance; CPE stands for the double-layer capacitance of the electrolyte/electrode interface, and the two parameters of CPE is defined as CPE-T and CPE-P;  $R_{ct}$  stands for the

charge transfer resistance; W represents the electrolyte diffusion capacitance in the electrode, and the three parameters of W is defined as W-R, W-T, and W-P. The parameters of each component in the equivalent circuit fitted by ZsimpWin software are reported in Table 4. As shown in Table 4 that under the overpotential where the redox reaction of  $\text{Fe}^{2+}/\text{Fe}^{3+}$  couple mainly takes place ( $\eta = 0.4 \text{ V}$ ), the relationship of  $R_{ct}$  values is  $R_{ct}(\text{T-CF}) > R_{ct}(\text{GF}) > R_{ct}(\text{CF}) > R_{ct}(\text{T-GF})$ . The more oxygen functional groups in the samples roughly, the smaller the  $R_{ct}$  value. However, T-CF with the least graphitization degree possesses the highest charge transfer resistance to the positive reaction. Thus, benefits with respect to electrochemical activity for  $\text{Fe}^{2+}/\text{Fe}^{3+}$  couple could not only be attributed to the oxygen functional groups.<sup>48</sup>

In the negative reaction of  $\text{Cr}^{3+}/\text{Cr}^{2+}$  couple, the relationship of  $R_{ct}$  values is  $R_{ct}(\text{T-CF}) > R_{ct}(\text{T-GF})$

$> R_{ct}(\text{CF}) > R_{ct}(\text{GF})$ . Although the reaction peak current of T-GF and T-CF is enhanced as a result of the oxygen functional groups and the specific surface area, the charge transfer resistance of negative reaction on the surface of GF and CF becomes smaller, which is likely to be related to the deposition of the catalyst. In the negative electrolyte environment,  $\text{BiCl}_3$  was introduced as the catalyst, and the catalytic process includes multisteps as follows<sup>6</sup>:



The influence of  $\text{Bi}^{3+}$  on the electrode reaction of  $\text{Cr}^{3+}/\text{Cr}^{2+}$  redox couple may be  $\text{Bi}^{3+}$  is first oxidized to Bi and then forms an intermediate  $\text{BiH}_x$  with  $\text{H}^+$ . Afterward,  $\text{BiH}_x$  does not decompose into  $\text{H}_2$  but participates in the reaction in which  $\text{Cr}^{3+}$  is reduced to  $\text{Cr}^{2+}$ . Therefore, the relatively complete carbon structure of the electrode is beneficial to the deposition of the catalyst. Based on the results of XRD and Raman analysis in the foregoing, it is known that the negative reaction catalyzed by  $\text{Bi}^{3+}$  obtains a smaller charge transfer resistance on the surfaces of GF and CF owing to the higher graphitization degree than T-GF and T-CF. It is worthy to note that the effect of hot air and Bi on GF and CF is dependent on their construction. That means, in the case of using GF or CF with different graphitization degree, GF and CF have different electrocatalytic activities through hot air and Bi. Therefore, it is inevitable that no consistent

treatment method can be found in the literature for the above characteristics of GF and CF.<sup>49-51</sup> The electrochemical characteristics of samples in positive reaction and negative reaction suggest that the electrode activity in the ICRFB is affected not only by the oxygen functional groups but also by the graphitization degree.

### 3.3 | Single cell performance

Figure 9 is the EE, CE, and VE of the ICRFBs assembled with each sample as the electrode. The current density during charge-discharge cycling is  $60 \text{ mA}\cdot\text{cm}^{-2}$ . The VE value of ICRFB is closely related to the electrochemical activity of electrodes, as the activity may directly involve the overall system polarization (not only the activation polarization but also consist of ohmic and concentration polarization).<sup>52,53</sup> During 30 cycles in Figure 9, the relationship of VE values is  $\text{VE}(\text{GF}) > \text{VE}(\text{T-GF}) > \text{VE}(\text{T-CF}) > \text{VE}(\text{CF})$ . The cell performance is not completely dependent on the electrochemical results of the positive or negative reaction, indicating that activation polarization is not the only main parameter affecting the ICRFB performance. The results in Figure 9A demonstrate that the poor performance of CF may be due to its low graphitization degree and the large ohmic loss. Therefore, GF exhibits much higher electrocatalytic activity than CF, for the dominant limitation in an ICRFB is ohmic polarization.<sup>9,14</sup> The thermal oxidation method can decrease the activation polarization loss by enlarging the BET and the number of oxygen functional groups in CF; hence, the EE value of T-CF is about 80% and relatively stable as shown in Figure 9B. However, the EE value of T-GF is about 86% owing to its higher graphitization

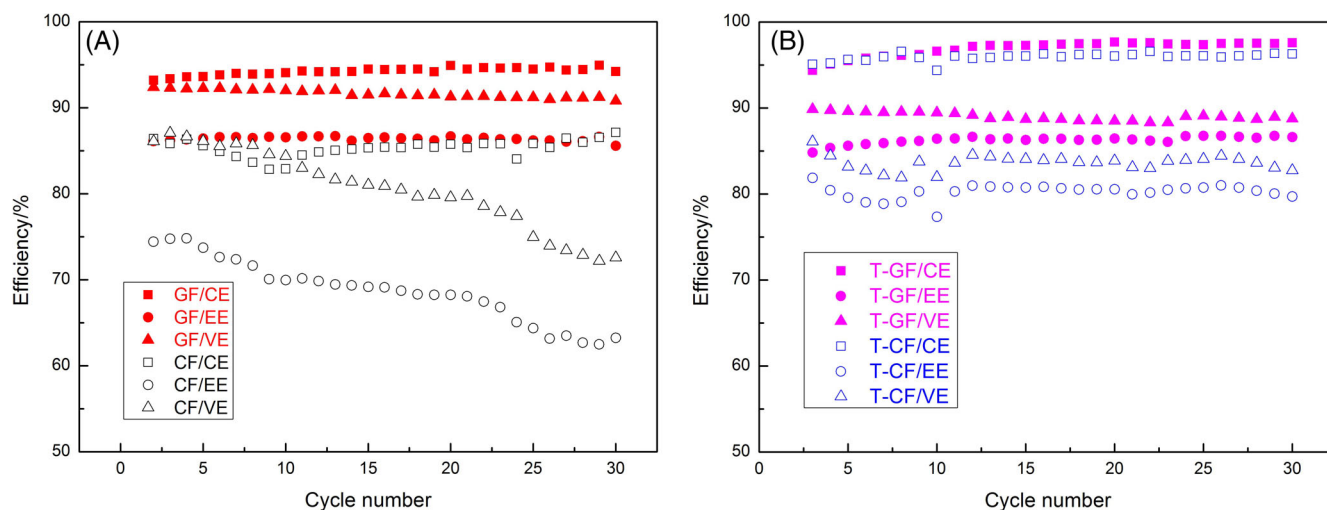


**FIGURE 9** Cell efficiency of (A) GF vs CF and (B) T-GF vs T-CF at  $60 \text{ mA}\cdot\text{cm}^{-2}$ . CF, carbon felt; GF, graphite felt [Colour figure can be viewed at [wileyonlinelibrary.com](http://wileyonlinelibrary.com)]

degree and oxygen functional groups, which indicates that the T-GF has good electrochemical kinetics than T-CF. Obviously, the ICRFBs assembled with GF and T-GF exhibit higher efficiency and better chemical stability. The VE value of GF is larger, about 92%, while that of T-GF is about 89%. The CE values of GF and T-GF are about 97% and 94% because of the combination of hot air and Bi catalyst, respectively. As a result, the EE values of GF and T-GF are similar, both of which are about 86% at a current density of  $60 \text{ mA}\cdot\text{cm}^{-2}$ . A comparison of the efficiencies of samples treated at different temperatures also showed a similar result (Table S2). CF pretreated at  $400^\circ\text{C}$  for 5 hours and at  $600^\circ\text{C}$  for 5 hours can also improve the energy efficiency compared with CF. Furthermore, the electrochemical activity of GF is better than GF pretreated at  $400^\circ\text{C}$  for 5 hours and at  $600^\circ\text{C}$  for 5 hours as well.

The long-time stability of the cells was shown in Figure 10. Figure 10A demonstrates the discharge

capacity attenuation of the ICRFBs at the charge-discharge current density of  $60 \text{ mA}\cdot\text{cm}^{-2}$ . The capacity loss of an ICRFB is more dependent on the reaction activity and the hydrogen evolution at the negative electrode.<sup>8,29,30</sup> In Figure 10A, the performance of T-GF and T-CF is more ideal than GF and CF in terms of the capacity decay rate. The capacity decay rate of T-GF and T-CF is around 1.26% capacity per cycle, while it is around 2.90% and 2.99% for GF and CF, respectively. In fact, the platform voltages of GF and CF are better than those of T-GF and T-CF after the first cycle (Figure 10B). The longer charge-discharge time of GF or CF causes more capacity decay during the 30th cycle (Figure 10C). The capacity attenuation rate for an ICRFB is primarily owing to the hydrogen evolution and the worse electrochemical kinetics of the negative reaction. Bismuth chloride is therefore added to the negative electrolyte as which we have taken, which inhibits hydrogen evolution and its catalysis effect is shown in the formula (5-7). There is still

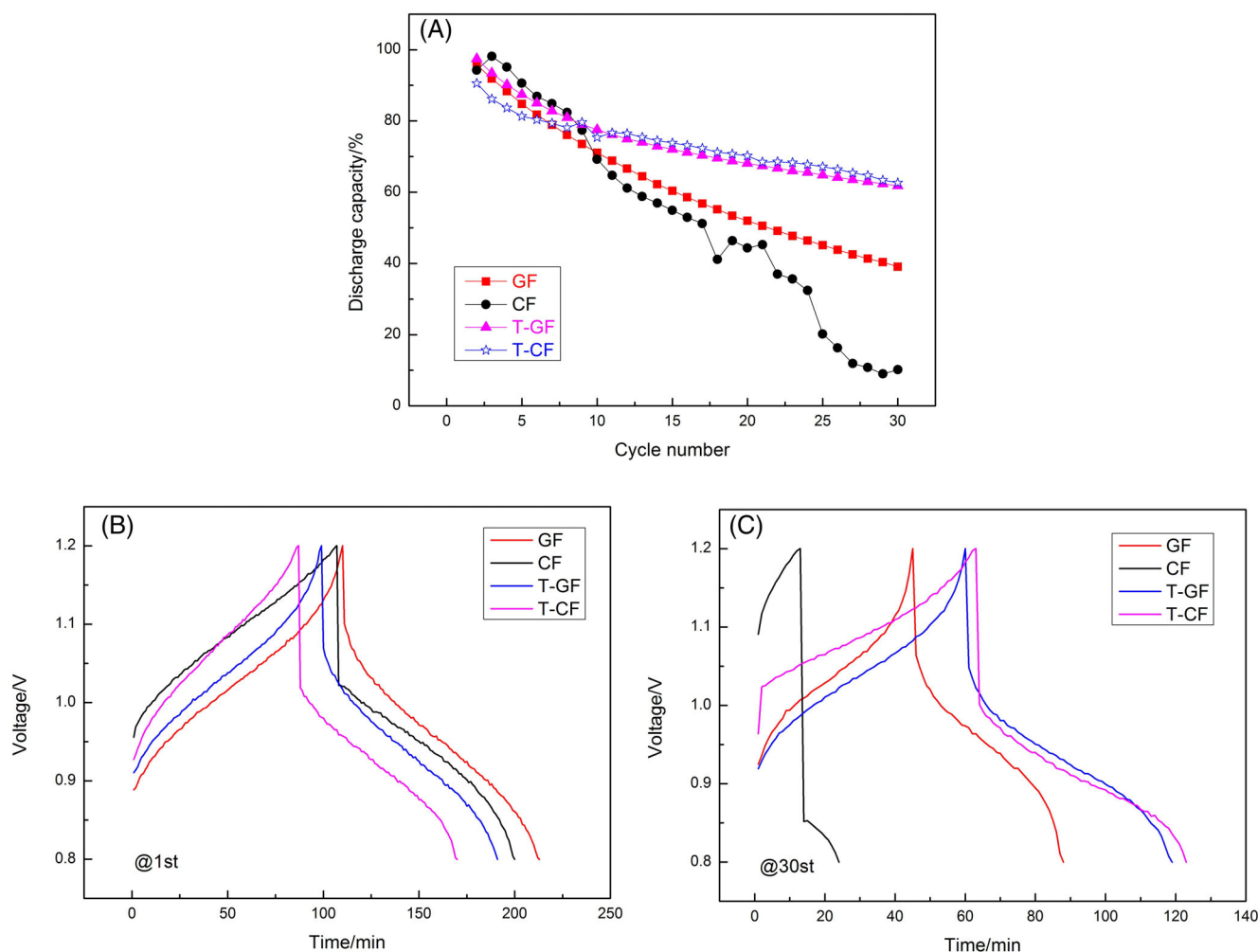
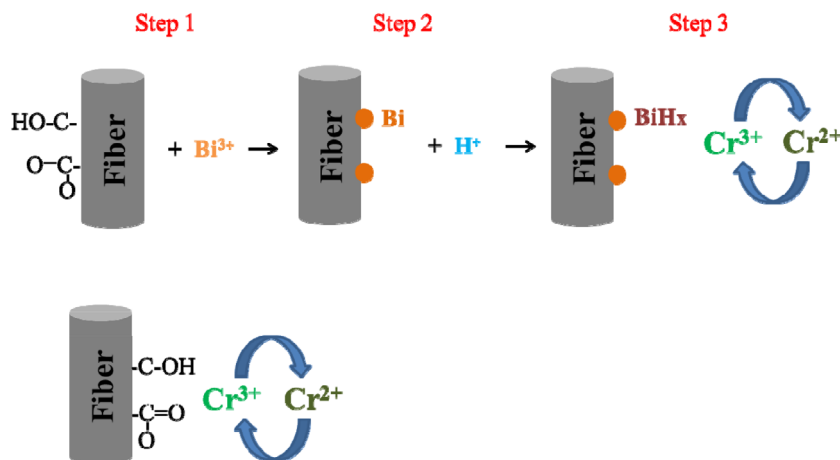


**FIGURE 10** (A) Discharge capacity retention and charge-discharge profiles for (b) first and (c) 30th cycle at  $60 \text{ mA}\cdot\text{cm}^{-2}$ . CF, carbon felt; GF, graphite felt [Colour figure can be viewed at [wileyonlinelibrary.com](http://wileyonlinelibrary.com)]

**SCHEME 3** The redox reaction mechanism for  $\text{Cr}^{3+}/\text{Cr}^{2+}$  couple through (A)  $\text{BiCl}_3$  and (B) oxygen functional groups [Colour figure can be viewed at [wileyonlinelibrary.com](http://wileyonlinelibrary.com)]



a higher rate of capacity attenuation in CF and GF during extended cycling, suggesting that the multistep catalytic process involving bismuth ions in the negative reaction is slow. At the same time, the oxygen functional groups in T-CF and T-GF could directly facilitate the  $\text{Cr}^{3+}/\text{Cr}^{2+}$  redox reaction in the electrolyte.<sup>54</sup> Moreover, the oxygen functional groups could promote the contact between electrode and bismuth ions. Thus, poor kinetics of chromium ions in the negative half-cell assembled with CF or GF causes accumulation of ferric ions in the positive half-cell, which results in an imbalance of state of charge (SOC) between negative and positive electrolytes, and brings on capacity attenuation quickly.<sup>55</sup>

Recently, there have been many attempts to modify the electrode through oxidation in VRFBs. It is well-known that oxygen functional groups are the essential factor to evaluate the electrode activity in VRFBs. As summarized in Table S1, it is clearly found that thermally treated electrodes and electrolyte involving bismuth ions are essential in ICRFBs. Although bismuth ions are considered to have the dual effect of inhibiting the hydrogen evolution reaction and catalyzing negative reaction, the shorter catalytic path by oxygen functional groups is beneficial to improve the stability of ICRFBs as shown in Scheme 3, which is rarely reported in previous work.<sup>6,9,10,28,30,54,55</sup>

## 4 | CONCLUSION

The thermally treated electrodes based on the commercial PAN-based GF and CF are successfully prepared at a temperature of  $500^\circ\text{C}$  for 5 hours. The difference of physiochemical properties between CF and GF and the effect of thermal treatment and catalyst ( $\text{BiCl}_3$ ) in the electrolyte on the electrochemical performance were investigated. CF is more easily oxidized by hot air, which is attributed to the GF possesses higher graphitization degree

than that of CF. Thus, the surface area of T-CF increases more significantly, which in turn causes a more decrease in the graphitization degree of T-CF than those of T-GF. However, the higher graphitization degree of GF also makes it easier to contain more edge oxygen functional groups. The electrochemical activities for GF and CF before and after the thermal treatment are directly related to the graphitization degree and oxygen functional groups. As a result, GF and T-GF exhibit much higher electrocatalytic activity than CF and T-CF, for the dominant limitation in an ICRFB is ohmic and activation polarization. The performance of T-GF and T-CF is more ideal in terms of capacity maintenance. Although bismuth ions are believed to have the dual effect of inhibiting the hydrogen evolution reaction and catalyzing the negative electrode reaction, the shorter catalytic path by oxygen functional groups is beneficial to improve the stability of ICRFBs. Therefore, GF after thermal activation together with the addition of  $\text{BiCl}_3$  in the electrolyte is a more promising electrode material for ICRFBs application than CF.

## ACKNOWLEDGEMENTS

This work was financially supported by National Natural Science Funds of China (Grant No. 51702144), the Fundamental Research Funds for the Colleges and Universities in Liaoning Province (2017LNQN15), and the Excellent Talent Training Program of University of Science and Technology Liaoning (2019RC04).

## ORCID

Huan Zhang <https://orcid.org/0000-0003-2284-4274>

Chuanyu Sun <https://orcid.org/0000-0003-4932-7787>

## REFERENCES

1. Zhang CK, Zhang LY, Ding Y, et al. Progress and prospects of next-generation redox flow batteries. *Energy Storage Materials*. 2018;15:324-350.

- Ding C, Zhang HM, Li XF, et al. Vanadium flow battery for energy storage: prospects and challenges. *The Journal of Physical Chemistry Letters*. 2013;4:1281-1294.
- Li XR, Xiong J, Tang A, et al. Investigation of the use of electrolyte viscosity for online state-of-charge monitoring design in vanadium redox flow battery. *Appl Energy*. 2018;211:1050-1059.
- Zeng YK, Li FH, Lu F, et al. A hierarchical interdigitated flow field design for scale-up of high-performance redox flow batteries. *Appl Energy*. 2019;238:435-441.
- C. Ponce de León, A. Frias-Ferrer, J. González-García, et al. Redox flow cells for energy conversion. *J Power Sources*, 2006, 160:716-732.
- Zhang H, Tan Y, Li JY, et al. Studies on properties of rayon- and polyacrylonitrile-based graphite felt electrodes affecting Fe/Cr redox flow battery performance. *Electrochim Acta*. 2017; 248:603-613.
- Lopez-Atalaya M, Codina G, Perez JR, Vazquez JL, Aldaz A. Optimization studies on a Fe/Cr redox flow batteries. *J Power Sources*. 1992;39:147-154.
- Yi BL, Liang BC, Zhang EJ, et al. Iron/chromium redox flow cell system. *Journal of Chemical Industry and Engineering*. 1992;3:330-336.
- Zeng YK, Zhao TS, Zhou XL, Zeng L, Wei L. The effects of design parameters on the charge-discharge performance of iron-chromium redox flow batteries. *Appl Energy*. 2016;182: 204-209.
- Zeng YK, Zhou XL, An L, Wei L, Zhao TS. A high-performance flow-field structured iron-chromium redox flow battery. *J Power Sources*. 2016;324:738-744.
- Sun CY, Zhang H, Luo XD, Chen N. A comparative study of Nafion and Sulfonated poly(ether ether ketone) membrane performance for iron-chromium redox flow battery. *Ionics*. 2019; 25:4219-4229.
- Y. Xiang, W. A. Daoud. Cr<sub>2</sub>O<sub>3</sub>-modified graphite felt as a novel positive electrode for vanadium redox flow battery. *Electrochim Acta*. 2018;290:176-184.
- Kim K, Park MS, Kim YJ, et al. A technology review of electrodes and reaction mechanisms in vanadium redox flow batteries. *J Mater Chem A*. 2015;3:16913-16933.
- Liu T, Li XF, Nie HJ, et al. Investigation on the effect of catalyst on the electrochemical performance of carbon felt and graphite felt for vanadium flow batteries. *J Power Sources*. 2015;286:73-81.
- Fizer E, Heine M. Carbon fibre manufacture and surface treatment composite[M]. *Amsterdam: Materials Veries Volume*. 1988;2:73-148.
- Tse-Hao KO. The influence of pyrolysis on physical properties and microstructure of modified PAN fibers during carbonization. *J Appl Polym Sci*. 1991;43:589-600.
- T. J. Rabbow, M. Trampert, P. Pokorny, P. Binder, A. H. Whitehead Variability within a single type of polyacrylonitrile-based graphite felt after thermal treatment. Part I: physical properties. *Electrochim Acta*, 2015, 173:17-23.
- Yu LH, Lin F, Xiao WD, et al. Achieving efficient and inexpensive vanadium flow battery by combining Ce<sub>x</sub>Zr<sub>1-x</sub>O<sub>2</sub> electrocatalyst and hydrocarbon membrane. *Chem Eng J*. 2019;356: 622-631.
- Wei GJ, Jia CK, Liu JG, et al. Carbon felt supported carbon nanotubes catalysts composite electrode for vanadium redox flow battery application. *J Power Sources*. 2012;220:185-192.
- Li WY, Liu JG, Yan CW, et al. Multi-walled carbon nanotubes used as an electrode reaction catalyst for VO<sup>2+</sup>/VO<sub>2</sub><sup>+</sup> for a vanadium redox flow battery. *Carbon*. 2011;49:3463-3470.
- Li B, Gu M, Nie ZM, et al. Bismuth nanoparticle decorating graphite felt as a high-performance electrode for an all-vanadium redox flow battery. *Nano Lett*. 2013;13:1330-1335.
- Zhang FF, Huang SP, Wang X, et al. Redox-targeted catalysis for vanadium redox-flow batteries. *Nano Energy*. 2018;52: 292-299.
- Pezeshki AM, Clement JT, Veith GM, Zawodzinski TA, Mench MM. High performance electrodes in vanadium redox flow batteries through oxygen-enriched thermal activation. *J Power Sources*. 2015;294:333-338.
- Jang J-K, Kim T-H, Yoon SJ, Lee JY, Lee J-C, Hong YT. Highly proton conductive, dense polybenzimidazole membranes with low permeability to vanadium and enhanced H<sub>2</sub>SO<sub>4</sub> absorption capability for use in vanadium redox flow batteries. *J Mater Chem A*. 2016;4:14342-14355.
- Shin HY, Cha MS, Hong SH, et al. Poly(p-phenylene)-based membrane materials with excellent cell efficiencies and durability for use in vanadium redox flow batteries. *J Mater Chem A*. 2017;5:12285-12296.
- Zeng YK, Yang ZF, Lu F, et al. A novel tin-bromine redox flow battery for large-scale energy storage. *Appl Energy*. 2019; 255. <https://doi.org/10.1016/j.apenergy.2019.113756>.
- Mehboob S, Ali G, Shin H-J, et al. Enhancing the performance of all-vanadium redox flow batteries by decorating carbon felt electrodes with SnO<sub>2</sub> nanoparticles. *Appl Energy*. 2018;229: 910-921.
- Zeng YK, Zhou XL, Zeng L, Yan XH, Zhao TS. Performance enhancement of iron-chromium redox flow batteries by employing interdigitated flow fields. *J Power Sources*. 2016;327: 258-264.
- Zeng YK, Zhao TS, Zhou XL, Zou J, Ren YX. A hydrogen-ferric ion rebalance cell operating at low hydrogen concentrations for capacity restoration of iron-chromium redox flow batteries. *J Power Sources*. 2017;352:77-82.
- Hollax E, Cheng DSH. The influence of oxidative pretreatment of graphite electrodes on the catalysis of the Cr<sup>3+</sup>/Cr<sup>2+</sup> and Fe<sup>3+</sup>/Fe<sup>2+</sup> redox reactions. *Carbon*. 1985;23(6):655-664.
- Sun CY, Zhang H. Investigation of Nafion series membranes on the performance of iron-chromium redox flow battery. *International Journal of Energy Research*. 2019;43:8739-8752.
- Sun CY, Zlotorowicz A, Nawn G, et al. [Nafion/(WO<sub>3</sub>)<sub>x</sub>] hybrid membranes for vanadium redox flow batteries. *Solid State Ion*. 2018;319:110-116.
- Sun CY, Negro E, Vezzù K, et al. Hybrid inorganic-organic proton-conducting membranes based on SPEEK doped with WO<sub>3</sub> nanoparticles for application in vanadium redox flow batteries. *Electrochim Acta*. 2019;309:311-325.
- Arenas LF, Carlos Ponce de León, frank C. Walsh. Pressure drop through platinized titanium porous electrodes for cerium-based redox flow batteries. *AIChE Journal*. 2018;64(3):1135-1146.
- Houska CR, Warren BE. X-ray study of the graphitization of carbon black. *J Appl Phys*. 1954;25:1503-1509.
- Matthew W, Ignacio MG, Jose VA, et al. The effect of graphitization temperature on the structure of helical-ribbon carbon nanofibers. *Carbon*. 2009;47:2211-2218.

37. Dixon D, Babu DJ, Langner J, et al. Effect of oxygen plasma treatment on the electrochemical performance of the rayon and polyacrylonitrile based carbon felt for the vanadium redox flow battery application. *J Power Sources*. 2016;332:240-248.
38. Sun C, Vezzù K, Pagot G, et al. Elucidation of the interplay between vanadium species and charge-discharge processes in VRFBs by Raman spectroscopy. *Electrochim Acta*. 2019;318:913-921.
39. Eifert L, Banerjee R, Jusys Z. Characterization of carbon felt electrodes for vanadium redox flow batteries: impact of treatment methods. *J Electrochem Soc*. 2018;165(11):2577-2586.
40. Kim J, Lim H, Jyoung J-Y, Lee E-S, Yi JS, Lee D. High electrocatalytic performance of N and O atomic co-functionalized carbon electrodes for vanadium redox flow battery. *Carbon*. 2017;111:592-601.
41. Yue ZR, Jiang W, Wang L, Gardner SD, Pittman CU Jr. Surface characterization of electrochemically oxidized carbon fiber. *Carbon*. 1999;37(11):1785-1796.
42. Abbas S, Lee H, Hwang J, et al. A novel approach for forming carbon nanorods on the surface of carbon felt electrode by catalytic etching for high-performance vanadium redox flow battery. *Carbon*. 2018;128:31-37.
43. Yao C, Zhang HM, Liu T, et al. Carbon paper coated with supported tungsten trioxide as novel electrode for all-vanadium flow battery. *J Power Sources*. 2012;218:455-461.
44. Park MS, Lee NJ, Lee SW, Kim KJ, Oh DJ, Kim YJ. High-energy redox-flow batteries with hybrid metal foam electrodes. *Applied Materials & Interfaces*. 2014;6:10729-10735.
45. Sun B, Skyllas-Kazacos M. Modification of graphite electrode materials for vanadium redox flow battery application-part I. thermal treatment. *Electrochim Acta*. 1992;37:1253-1260.
46. Sun B, Skyllas-Kazacos M. Chemical modification for graphite electrode materials for vanadium redox flow battery application-part II. Acid treatment. *Electrochim Acta*. 1992;37:2459-2465.
47. Mazúr P, Mrlík J, Beneš J, et al. Performance evaluation of thermally treated graphite felt electrodes for vanadium redox flow battery and their four-point single cell characterization. *J Power Sources*. 2018;380:105-114.
48. Ghimire PC, Schweiss R, Scherer GG, Lim TM, Wai N, Bhattarai A, Yan Q. Optimization of thermal oxidation of electrodes for the performance enhancement in all-vanadium redox flow battery. *Carbon*. 2019;155:176-185.
49. Zhou HP, Xi JY, Li ZH, et al. CeO<sub>2</sub> decorated graphite felt as a high-performance electrode for vanadium redox flow batteries. *RSC Adv*. 2014;4:61912-61918.
50. TJ Rabbow, M Trampert, P Pokorny, P Binder, AH Whitehead Variability within a single type of polyacrylonitrile-based graphite felt after thermal treatment. Part I: physical properties. *Electrochim Acta*. 2015;173:17-23.
51. TJ Rabbow, M Trampert, P Pokorny, P Binder, AH Whitehead Variability within a single type of polyacrylonitrile-based graphite felt after thermal treatment. Part II: chemical properties. *Electrochim Acta*. 2015;173:24-30.
52. Schweiss R. Influence of bulk fibre properties of PAN-based carbon felts on their performance in vanadium redox flow batteries. *J Power Sources*. 2015;278:308-313.
53. Zhou XL, Zeng YK, Zhu XB, Wei L, Zhao TS. A high-performance dual-scale porous electrode for vanadium redox flow batteries. *J Power Sources*. 2016;325:329-336.
54. Liu B, Liu S, He Z, et al. Improving the performance of negative electrode for vanadium redox flow battery by decorating bis-muth hydrogen edetate complex on carbon felt. *Ionics*. 2019;25:4231-4241.
55. Zeng YK, Zhao TS, An L, Zhou XL, Wei L. A comparative study of all-vanadium and iron-chromium redox flow batteries for large-scale energy storage. *J Power Sources*. 2015;300:438-443.

## SUPPORTING INFORMATION

Additional supporting information may be found online in the Supporting Information section at the end of this article.

**How to cite this article:** Zhang H, Chen N, Sun C, Luo X. Investigations on physicochemical properties and electrochemical performance of graphite felt and carbon felt for iron-chromium redox flow battery. *Int J Energy Res*. 2020;1-15. <https://doi.org/10.1002/er.5179>